Hydraulically Amplified Terfenol-D Actuator for Adaptive Powertrain Mounts

Suryarghya Chakrabarti
e-mail: chakrabarti.3@osu.edu

Marcelo J. Dapino[1]
e-mail: dapino.1@osu.edu

Smart Vehicle Concepts Center,
Department of Mechanical and
Aerospace Engineering,
The Ohio State University,
Columbus, OH 43210

A magnetostrictive actuator with a stroke of ±1 mm and a blocked force of ±25 N has been developed based on a Terfenol-D driver and a hydraulic stroke amplification mechanism. A mechanical model for this magneto-hydraulic actuator (MHA) is formulated by combining linear piezomagnetic relations for Terfenol-D and a lumped parameter mechanical system model describing the system vibrations. Friction at the fluid seals is described by the LuGre model. The model accurately describes the frequency-domain behavior of the actuator in mechanically-blocked and mechanically-free conditions. The MHA is benchmarked against a commercial electromagnetic driver used in active powertrain mounts in terms of mechanical performance (blocked force and unloaded displacement) and electrical power consumption. Measurements show that the MHA achieves more than twice the frequency bandwidth of the commercial device in the free displacement response, along with comparable static displacements. The commercial device produces higher blocked forces in the frequency range of 10 Hz to 120 Hz beyond which the generated forces are comparable up to 400 Hz. Spectral analysis reveals significant second order components in the commercial actuator displacement response which are absent in the MHA. Further, the MHA achieves superior performance than the commercial actuator operated at maximum current (6 A) with power consumption identical to that of the commercial actuator operated at minimum current (4 A). [DOI: 10.1115/1.4004669]

1 Introduction

An automotive engine mount has two main purposes. First, to isolate the chassis from engine vibrations and second, to prevent engine bounce from road excitations or sudden braking and acceleration. The frequency range of engine vibrations depends on the number of cylinders in the engine, the stroke number, and the engine speed. It has been established that for a four-cylinder, four-stroke engine the frequency of engine vibrations ranges from 20 to 200 Hz for engine speeds of 600–6000 rpm [1]. For an eight-cylinder engine the frequency of vibrations would be 40–400 Hz for the same range of engine speeds. In order for a mount to be effective in isolating the chassis from engine vibrations, it should be compliant and lightly damped to reduce force transmissibility. Shock excitations associated with road roughness or sudden acceleration and braking typically occur below 5 Hz with much higher amplitudes than engine vibrations. To prevent excessive engine bounce due to such excitations, the mount should be stiff and heavily damped.

An ideal engine mount would have frequency and amplitude dependent stiffness characteristics. Despite advances in passive mount design (see, e.g., Yu et al. [1] and Jazar et al. [2]), the trend of increased engine power combined with lighter vehicle frames poses vibration isolation problems which passive mounts alone cannot adequately address. Hence, significant emphasis is now placed on investigating designs and methods to develop effective active mounts.

An active mount consists of a passive hydro-mount combined with an actuator which modulates the pressure of the hydraulic fluid in order to reduce the mount's force transmissibility. The isolation ability of an active mount strongly depends on the performance of the drive actuator. Lee et al. [3] developed an electromagnetic actuator with a bandwidth of 75 Hz. Gennesseaux [4] presented a variable-reluctance linear electric motor with built-in close loop control to address actuator nonlinearities. Matsuoka et al. [5] developed an active control engine mount to isolate the vibrations of a 3-liter V6 cylinder-on-demand engine when operated in three-cylinder mode at low rpm. Although active mounts with electromagnetic actuators can achieve significant vibration reduction, frequency bandwidths above 80 Hz are difficult to achieve with these designs. To achieve broader frequency bandwidth, actuators using smart material drivers have been considered.

Since smart materials capable of broadband response produce a stroke below mount requirements, the implementation of these materials in active mounts requires stroke amplification. Niezrecki et al. [6] have discussed displacement amplification techniques found in the literature. Mechanical amplification based on stacking or levers typically is too bulky to be used in active mount design. Another way to amplify the motion of smart material actuators is through hydraulic gain. The simplest way to achieve hydraulic amplification is to use pistons of different areas with the smart material driving the large piston and the power output delivered by the smaller driven piston. Yoon et al. [7] developed a piezo-driven actuator that uses this principle. Their device achieved a stroke of up to 1.3 mm with a blocked force of up to 6.5 N. Hydraulic amplification can also be achieved with smart material pumps driven at high frequency along with fluid rectification valves. Various pumps have been developed which utilize either magnetostrictive [8–10] or piezoelectric materials [11,12]. The current designs are too bulky and complex for use in engine mounts due to the presence of various pumping components-accumulator, check valves, direction control valve, and piston-type hydraulic actuator. Hence, direct hydraulic amplification mechanisms based on area ratios are more attractive for automotive engine mounts.

Ushijima and Kumakawa [13] developed a piezo-hydraulic actuator with a stroke of 70 μm which uses the hydraulic fluid in the mount for amplification. Shibayama et al. [14] developed a hydraulically amplified piezo actuator with a stroke of 0.3 mm in which the amplification fluid was separately sealed from the fluid in the mount.

[1]Corresponding author.

Contributed by the Technical Committee on Vibration and Sound to the JOURNAL OF VIBRATION AND ACOUSTICS. Manuscript received November 11, 2010; final manuscript received April 13, 2011; published online November 28, 2011. Assoc. Editor: Jeffrey Vipperman.

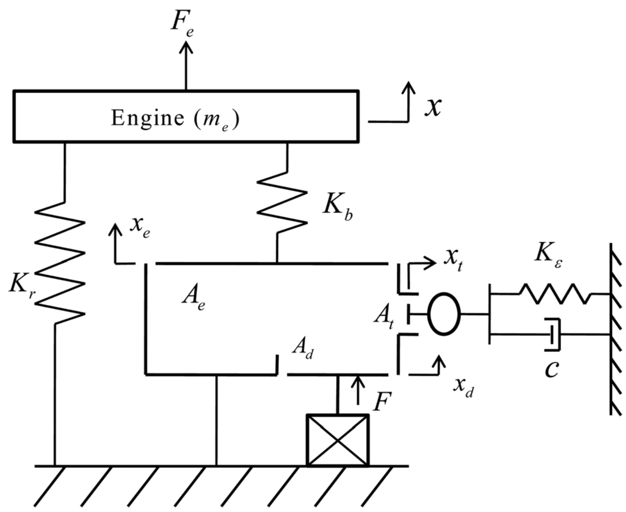

Fig. 1 Schematic of the active mount model (Lee et al. [3])

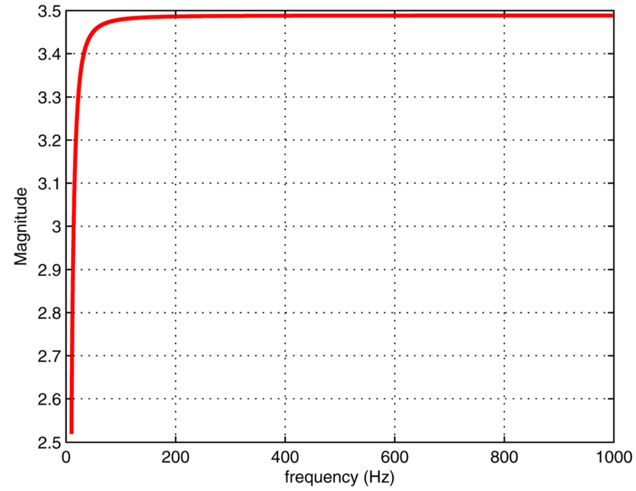

Fig. 2 Magnitude of transfer function $X_d/X(s)$

The objective of this study is to develop a compact bidirectional magneto-hydraulic actuator driven with Terfenol-D for active engine mounts. Calculation of the area ratio needed to achieve zero force transmissibility is presented in Section 2. With these design guidelines, a nonlinear model for the MHA is developed in Section 3. Calculated and measured responses in the frequency domain are compared in Section 4. In Section 5, the MHA is benchmarked against a commercial electrodynamic actuator used in active engine mounts. Both devices are tested in mechanically-free and mechanically-blocked conditions, and their responses are compared in terms of electrical power consumption, frequency bandwidth, and spectral content.

2 Actuator Design

2.1 Estimation of Actuator Requirements. To estimate the requirements imposed on an actuator used to drive active mounts, a lumped-parameter model similar to that presented by Lee et al. [3] is employed, as shown in Fig. 1. Model parameters are shown in Table 1. In this model, the transfer function actuator displacement over engine displacement is given by

$$\frac{X_d}{X}(s) = \left[\left(1+\frac{K_r}{K_b}\right)\frac{A_e}{A_d} + \frac{K_r A_t^2}{A_e A_d (ms^2+cs+K_\varepsilon)}\right] \tag{1}$$

and the transfer function actuator force over engine displacement is

$$\frac{F}{X}(s) = \left(\frac{A_d}{A_e}\right)K_r \tag{2}$$

which is obtained by equating the net transmitted force on the base to zero.

Table 1 Design parameters for the active mount

Parameter	Value
Main rubber stiffness (K_r)	127.4×10^3 N/m
Bulge stiffness of the rubber (K_b)	313.6×10^3 N/m
Compliance of the lower chamber (K_ε)	2.0 N/m
Equivalent cross-sectional area of the upper chamber (A_e)	4123 mm^2
Decoupler area	1662 mm^2
Cross-sectional area of the inertia track	50 mm^2
Fluid mass in the inertia track (m)	12.5 g
Damping coefficient in the inertia track	0.08 Ns/m

Figure 2 shows the magnitude of the frequency response function $X_d/X(s)$. Assuming harmonic engine displacement, its amplitude must be estimated in order to quantify X_d from (1) and F from (2). Holt and Rao [15] assumed engine vibrations of amplitude 0.3 mm over the range 0 to 100 Hz and 0.01 mm over the range 100 to 200 Hz. Ohadi and Maghsoodi [16] assumed an excitation of 1.0 mm in the frequency range 0 to 6 Hz and 0.05 mm at higher frequencies. Lee et al. [3] measured the engine vibration at idling conditions to be 0.22 mm. Kyprianou et al. [17] assumed excitations with rms amplitudes ranging from 0.005 mm at higher frequencies to 0.33 mm at lower frequencies. We assume the engine vibration amplitude as 0.5 mm at the idling frequency (20 Hz), decaying linearly to 0.1 mm at 100 Hz and then decreasing linearly to 0.05 mm at 1000 Hz [18]. The actuator displacement requirement calculated from (1) is 1.6 mm at 20 Hz, 0.35 mm at 100 Hz, and 0.175 mm at 1000 Hz. It is emphasized that these displacement requirements are for complete cancellation of the engine vibrations. Smart actuators with lower displacement output could also provide significant (although not complete) vibration reduction.

The stroke of the MHA is determined by the dimensional constraints on the Terfenol-D driver. In this case, a cylindrical Terfenol-D rod of diameter 0.5 in. (12.7 mm) and length 2 in. (50.8 mm) is chosen. The approximate blocking force produced by the rod is 4560 N (assuming E = 30 GPa), and the unloaded stroke is 60 μm (assuming λ = 1200 ppm).

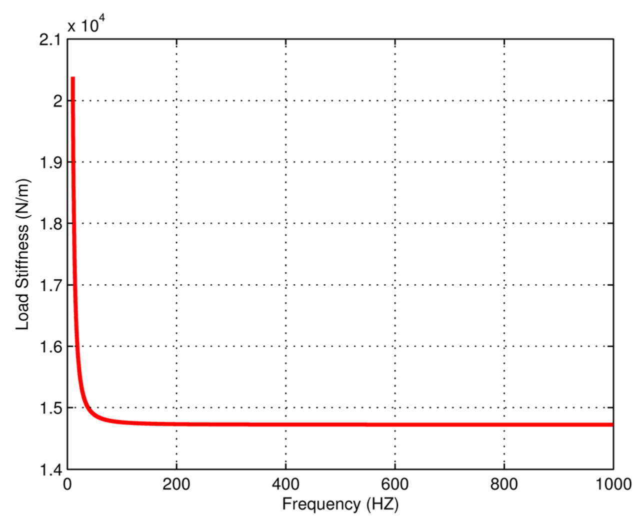

Fig. 3 Magnitude of load stiffness transfer function $F/X_d(s)$

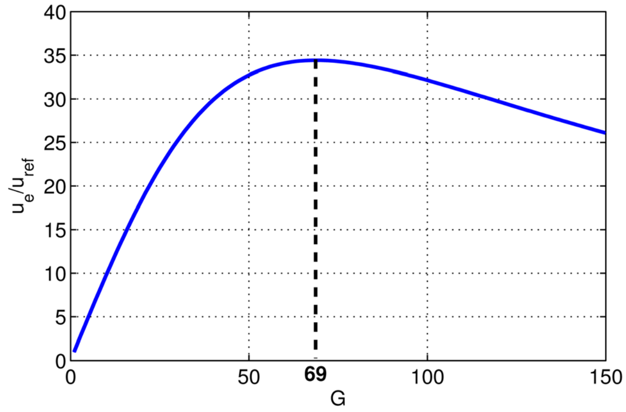

Fig. 4 Normalized stroke u_e/u_{ref} versus kinematic gain G

2.2 Actuator Gain. The calculation of kinematic gain for a smart actuator must incorporate loading effects since the maximum strain is obtained when the load is zero and the maximum load is supported when the displacement is zero. The stroke of a displacement-amplified smart actuator was derived by Giurgiutiu et al. [19],

$$\frac{u_e}{u_{\rm ref}} = \frac{G}{1 + rG^2} \tag{3}$$

where G is the kinematic gain, r is the ratio of load stiffness to the smart material rod stiffness, and $u_{\rm ref}$ is the unloaded displacement of the smart material driver. For a given r, the value of G which maximizes the stroke can be obtained by differentiating (3) with respect to G and equating to 0. This gives the design gain $G_{\rm opt}$ as

$$G_{\rm opt} = 1/\sqrt{r} \tag{4}$$

Division of (2) by (1) yields the effective stiffness of the load as seen by the driver (Fig. 3). To calculate $G_{\rm opt}$, the value of r at idling frequency is selected because the engine vibration amplitude is maximum at idling. The design gain $G_{\rm opt}$ is 69 as shown in Fig. 4. The exact area ratio of pistons in the final design is 69.6.

2.3 Magnetic Circuit and Preload. The magnetic circuit consists of three cylindrical Alnico permanent magnets of ID 1.125 in (28.575 mm) and OD 1.5 in (38.1 mm), an AWG 20 wire coil for generating the dynamic field, iron pieces for flux return and a Terfenol-D cylindrical rod. The coil has an ID of 0.6 in (15.24 mm) and an OD of 1 in (25.4 mm). Alnico magnets are selected because they provide an optimum level of bias field (≈ 40 kA/m) on the Terfenol-D rod in order to achieve symmetric bidirectional motion. Figure 5 shows the physical actuator and a cutout showing the various components.

The mechanical preload on the Terfenol-D rod is created by a wave spring situated above the driven piston and by a disc spring located between the magnetic circuit and drive piston. The force produced by the wave spring on the rod is magnified by the fluid. One advantage of this configuration is that the fluid remains in compression during operation; thus reducing the chances of cavitation. The wave spring should be able to produce the desired preload force, yet it must be as compliant as possible to produce little force variation over a large range of deformation (approximately ±1 mm) so that little energy from the Terfenol-D driver is used in compressing the spring. The fluid is sealed by two o-rings (#6 on the smaller piston and #32 for the larger piston). Table 2 lists the specifications for different actuator components.

3 Modeling

A three-degree-of-freedom dynamic model is developed as shown in Fig. 6. Each of the two pistons is assigned a degree of freedom (x_p and x_L). The support structure has a finite stiffness and hence a third degree of freedom (x_s) is used to model its displacement. The Terfenol-D rod extension is then computed by subtracting the support structure displacement from the drive piston displacement, $x_p - x_s$. Assuming no compliance of the fluid chamber, at any given instant of time the volumetric displacement of the hydraulic fluid is

$$\Delta V = A_p x_p - A_L x_L \tag{5}$$

The volumetric stiffness of the different elements in the fluid chamber plays a critical role in the performance of the MHA. Hence, a volumetric stiffness coefficient (C_o) is introduced, which yields the volumetric change as

$$\Delta V = A_p x_p - A_L x_L - \frac{\Delta p}{C_o} \tag{6}$$

The pressure in the fluid Δp can be linearized for small volumetric changes as follows,

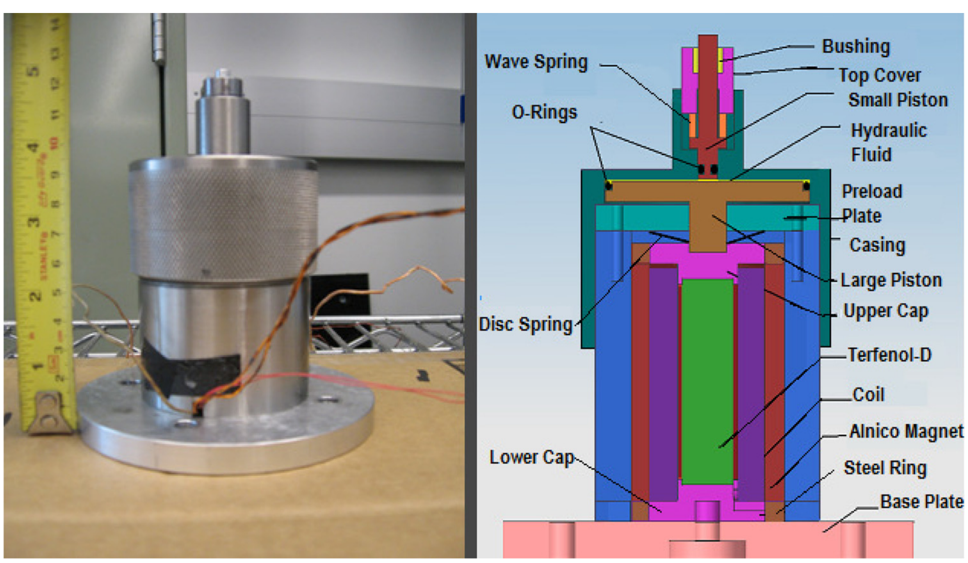

Fig. 5 Physical actuator (left) and cutout (right)

Table 2 List of Terfenol-D actuator components

Component	Specification
Length of Terfenol-D rod	2 in (50.8 mm)
Diameter of Terfenol-D rod	0.5 in (12.7 mm)
Alnico magnet (ID × OD × L)	(1.125 in (28.58 mm) × 1.5 in (38.1 mm) × 2.25 in (57.15 mm))
Mass of drive piston	74.67 g
Mass of driven piston	2.30 g
Volume of fluid (DTE 25)	1.30 c.c
Wave spring stiffness	3.5×10^3 N/m
Finger disc spring Stiffness	2.25×10^5 N/m

$$\Delta p = \beta \frac{\Delta V}{V_{\text{ref}}} \tag{7}$$

Combination of (6) and (7) gives

$$\Delta p = \underbrace{\left(\frac{C_o \beta}{C_o V_{\text{ref}} + \beta}\right)}_{\beta_{\text{eff}}} (A_p x_p - A_L x_L) \tag{8}$$

where β_{eff} is the effective volumetric modulus of the fluid and fluid chamber components. If the volumetric stiffness C_o of the chamber is very large then $\beta_{\text{eff}} \approx \beta/V_{\text{ref}}$. Further reduction in actuator performance is expected due to friction at the o-ring seals (particularly at the driven piston). Seal friction is quantified using the LuGre model for lubricated contacts [20] which describes the frictional force based on the bristle interpretation of friction. The LuGre model equations are given by

$$\frac{dz}{dt} = v - \sigma_0 \frac{|v|}{g(v)} z \tag{9}$$

$$g(v) = F_c + (F_s - F_c) e^{-(v/v_s)^2} \tag{10}$$

$$F_r = \sigma_0 z + \sigma_1(v) \frac{dz}{dt} + \sigma_2 v \tag{11}$$

$$\sigma_1(v) = \sigma_1 e^{-(v/v_d)^2} \tag{12}$$

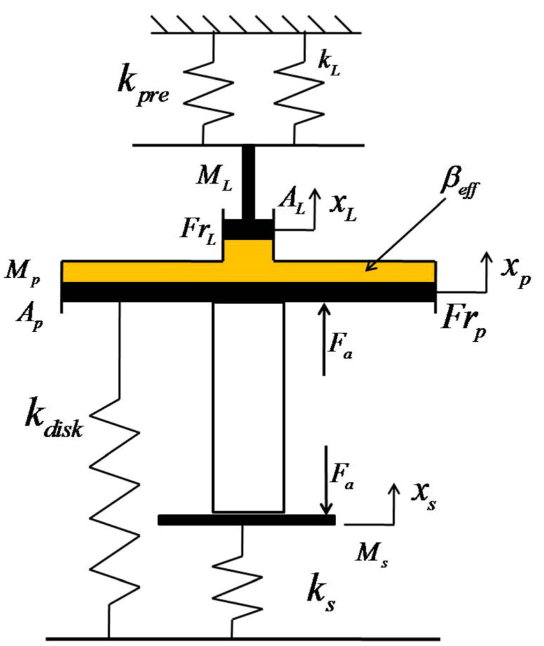

Fig. 6 Vibratory model for the magneto-hydraulic actuator

Here, z is the average bristle deflection, F_s and F_c are the static and coulomb frictional forces and σ_0, σ_1, and σ_2 are the bristle stiffness, bristle damping, and viscous damping coefficient, respectively. Parameter v_s is the Stribeck velocity and v_d is an additional parameter which controls the velocity dependence of $\sigma_1(v)$. The linear constitutive magnetomechanical relations for the Terfenol-D rod with field H and stress σ applied along the axial direction can be written as

$$\varepsilon = \frac{\sigma}{E^H} + dH \tag{13}$$

$$B = d\sigma + \mu^\sigma H \tag{14}$$

where, E^H is the Young's modulus at constant field and μ^σ is the magnetic permeability at constant stress. The force generated by a Terfenol-D rod with cross-sectional area A is

$$F_a = -\sigma A = E^H A dH - E^H A \frac{x_p - x_s}{l_a} \tag{15}$$

Substitution $H = NI/l_a$ gives

$$F_a = \underbrace{\left(\frac{E^H A}{l_a}\right)}_{k_a} dNI - E^H A \frac{(x_p - x_s)}{l_a} = \underbrace{(dk_a N)}_{\theta} I - k_a (x_p - x_s) \tag{16}$$

The equations of motion for the two pistons and the support structure are

$$M_p \ddot{x}_p + (k_{\text{disk}}) x_p + Fr_p = -\Delta p A_p + F_a \tag{17}$$

$$M_L \ddot{x}_L + (k_L + k_{\text{pre}}) x_L + Fr_L = \Delta p A_L \tag{18}$$

$$M_s \ddot{x}_s + k_s x_s = -F_a \tag{19}$$

Here, Fr_L and Fr_p are the friction forces at the driven and drive piston, respectively, obtained from the LuGre model. The electrical properties of the actuator can be modeled by expressing the voltage drop U across the drive coil as a sum of resistive and inductive components,

$$U = RI + NA\left(\frac{dB}{dt}\right) \tag{20}$$

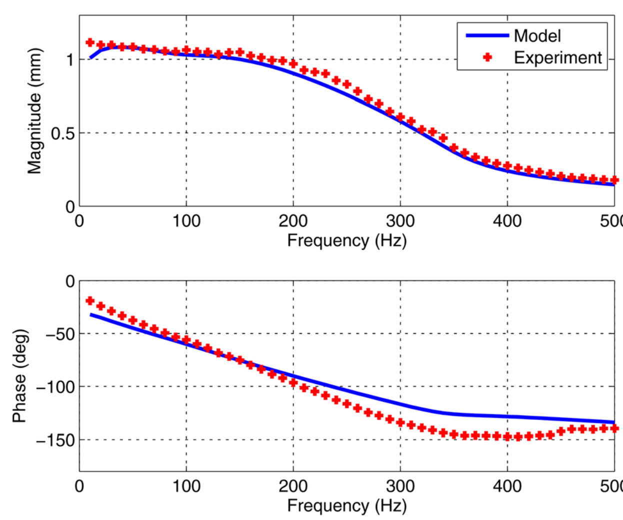

Fig. 7 Bode plot of transfer function driven-piston displacement over drive current, mechanically-free condition

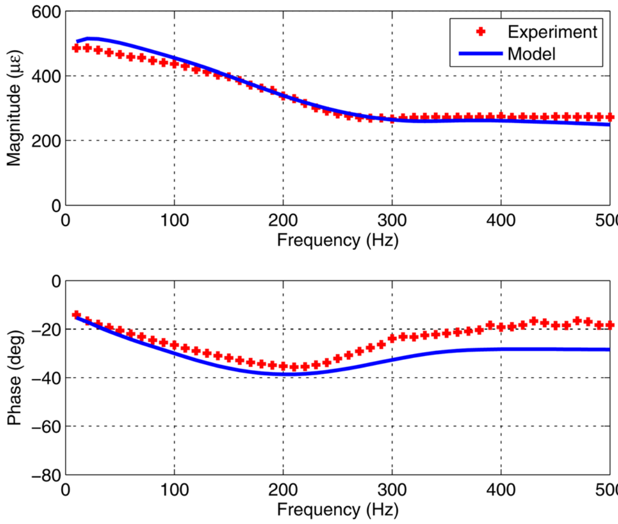

Fig. 8 Bode plot of transfer function Terfenol-D strain over drive current, mechanically-free condition

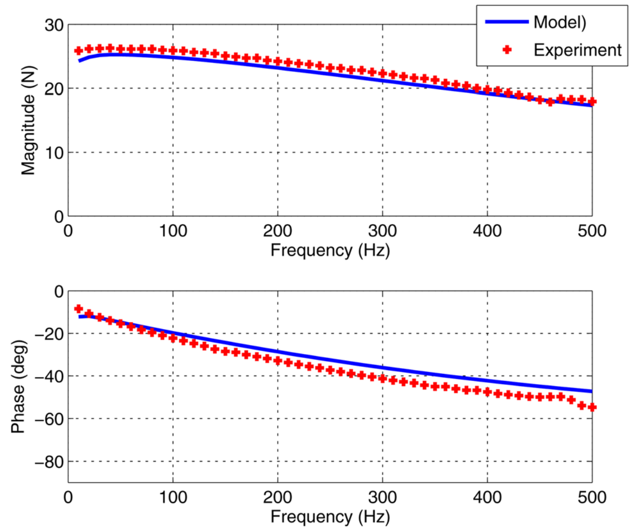

Fig. 10 Bode plot of transfer function blocked force over drive current, mechanically-blocked condition

Substitution of B from (14) gives

$$U = RI + \frac{\mu^\sigma N^2 A}{l}\left(1 - \frac{E^H d^2}{\mu^\sigma}\right)\left(\frac{dI}{dt}\right) + \theta\left(\frac{dx_p}{dt} - \frac{dx_s}{dt}\right) \tag{21}$$

The last term in (21) describes the effect of structural dynamics on the electrical properties of the system.

Before solving the system of equations, the volumetric modulus (β_{eff}) and LuGre model parameters (σ_0, σ_1, σ_2, v_s, v_d, F_s, and F_c) must be estimated. Parameter β_{eff} is determined from the generated blocked-force magnitudes and Terfenol-D strain under quasi-static conditions. The LuGre parameters for the drive piston's seal are estimated by comparing the time domain results for the blocked condition to experimental data at discrete frequencies. The driven piston being blocked does not play a role in the dynamics of the system. Once the parameters for the drive piston seal have been determined, the time domain displacement responses of the MHA in the free condition are compared to experimental data at discrete frequencies to determine the LuGre model parameters for the driven piston. Once the parameters have been identified, the system of equations is solved numerically at discrete actuation frequencies from 10 to 500 Hz in steps of 10 Hz. The frequency domain results are obtained by computing the Fast Fourier Transform of the steady state time domain solutions and plotting the magnitude and phase of the first-order component.

4 Model Results and Discussion

In this section, the basic response of the MHA is established under mechanically-free and mechanically-blocked conditions. The former response describes the ability of the actuator to generate maximum deflection (zero-force condition) whereas the latter describes the generation of force as the actuator is prevented from deflecting (zero-deformation condition). Under normal conditions, the MHA operates between these two extreme cases.

To describe the mechanically-free condition, the load stiffness k_L is set to 0. Figures 7–9 show model results and experimental measurements in the frequency domain for the output pushrod displacement, Terfenol-D strain, and electrical impedance, respectively. In all cases, the model was run with the same set of parameters. The model accurately describes the overall trends in the Bode plots. The discrepancy between the model and measurements is attributed

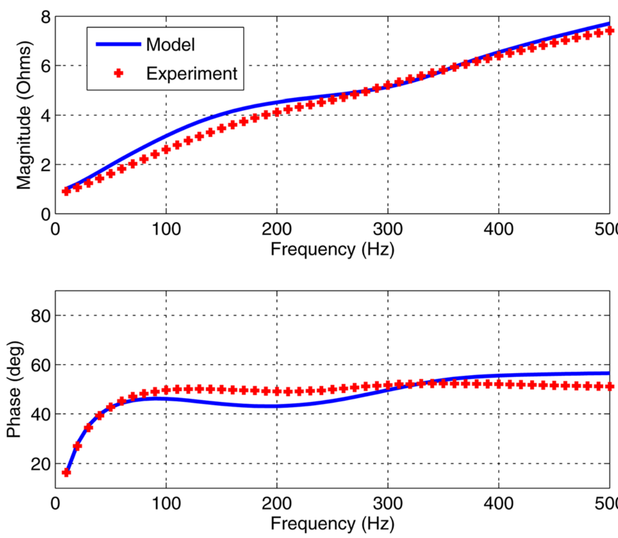

Fig. 9 Bode plot of electrical impedance transfer function, mechanically-free condition

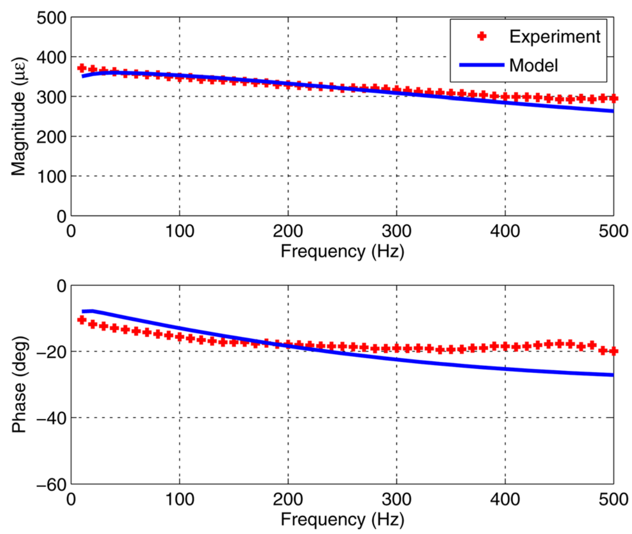

Fig. 11 Bode plot of transfer function Terfenol-D strain over drive current, mechanically-blocked condition

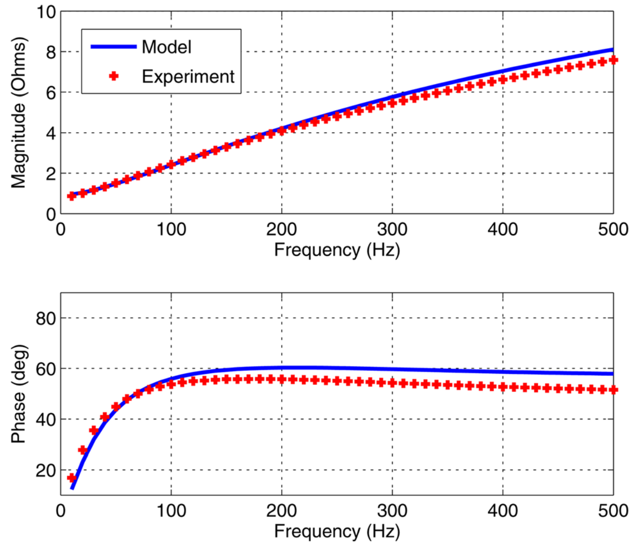

Fig. 12 Bode plot of electrical impedance transfer function, mechanically blocked condition

to unmodeled physics associated with hysteresis and nonlinearities in the driver and to complexity of the friction mechanics at the seals. It is emphasized that the loss in accuracy associated with the linear model is justified by the simplicity of the model equations, especially in the context of design and control applications.

To describe the mechanically-blocked condition, the output pushrod displacement is forced to be zero. This assumption reduces the model by one degree of freedom. All other parameters are kept the same as in the mechanically-free condition. Figures 10–12 show model results and experimental measurements in the frequency domain for blocked force, Terfenol-D strain, and electrical impedance. The model results are more accurate in this case due to the absence of complicated friction dynamics at the driven piston. The slight decrease in the blocked force at higher frequency is due to viscous damping at the driven piston seal. An important feature of the result is the large difference in phase between the Terfenol-D strain and the force output. This is described by the model due to the finite stiffness of the support structure. Had the support structure stiffness not been considered,

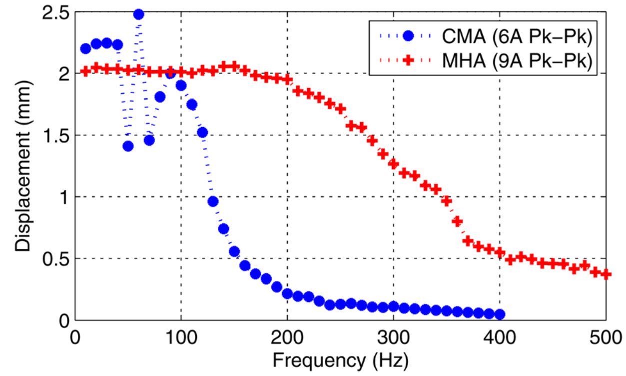

Fig. 14 Displacement in mechanically-free condition with both devices driven at full power

the phase of the Terfenol-D strain and the generated force would be the same since the fluid and fluid chamber components have been modeled as a constant-stiffness spring.

5 Comparative Study

The MHA is benchmarked against an electrodynamic mount actuator used in the Honda Odyssey. The commercial mount actuator is referred to as CMA. Both devices are tested under mechanically-free and mechanically-blocked conditions. The MHA is driven by a current of 9 A pk-pk with no bias while the CMA is driven at 6 A pk-pk with a 3 A dc bias, which corresponds to the upper limit of the current specifications for this device. All tests in the frequency domain are conducted at constant current through the use of a controller (Fig. 13). The controller uses the amplifier's current monitor and a feedback loop to adjust the output of the signal generator in order to drive the actuator with a specified constant current.

5.1 Mechanically-Free (Zero Force) Displacement. Figure 14 shows the pk-pk unloaded displacement for both devices, obtained by running histogram tests at discrete frequencies from 10 to 500 Hz and measuring the actuator output with a laser displacement sensor. While sine sweeps are typically preferred for

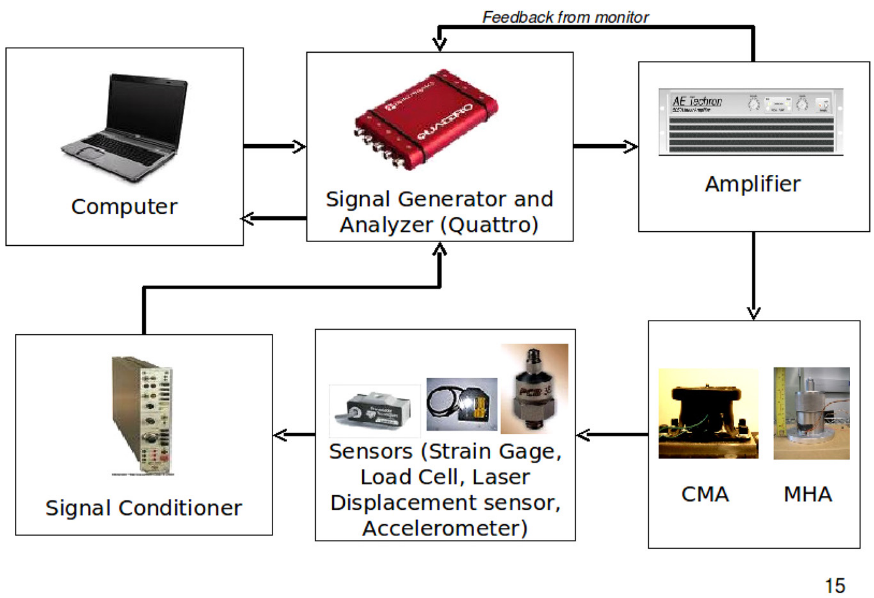

Fig. 13 Experimental setup used for current-controlled actuator tests

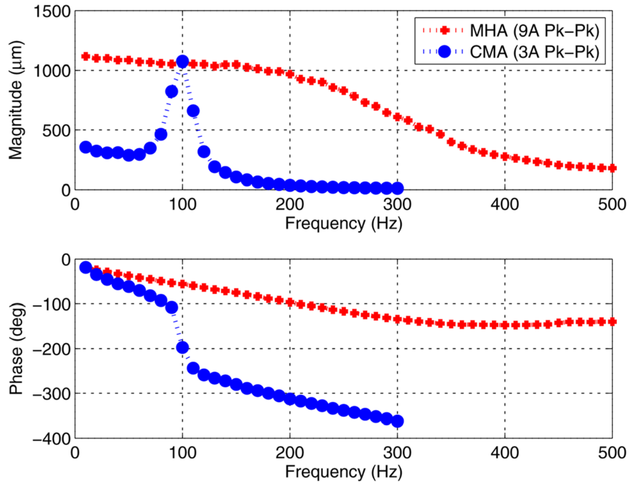

Fig. 15 Displacement in mechanically-free condition with the CMA driven at reduced power in order to allow for excitation through the 100 Hz resonance without damaging it

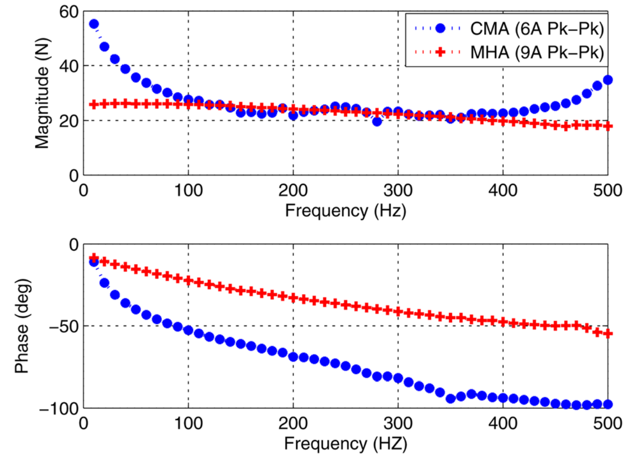

Fig. 17 Measured force response in mechanically-blocked condition

this type of testing, the CMA exhibits a resonance around 100 Hz where the pushrod slams the base of the mount making it difficult to use the controller with the frequency sweep test. In Fig. 15 the CMA is driven at a reduced power level (3 A pk-pk), which made it possible to conduct a frequency sweep test with the controller, showing the 100 Hz resonance. The response at full power shows that the MHA has a 3-dB cutoff of 280 Hz compared with a 110 Hz cutoff for the CMA. The gain-bandwidth products are 575 mm Hz and 274 mm Hz, respectively. The lack of ripple in the pass-band observed in the MHA is key for being able to control the force in the mount.

Figures 16(*a*) and 16(*b*) show the first three harmonics for each of the two free-displacement responses. The MHA exhibits a flat response over the frequency band considered, with a strong first-order harmonic and almost nonexistent second and third harmonics. This linear response is advantageous for control purposes. Conversely, the CMA exhibits significant distortion due to second and third harmonics. An actuator which has significant higher harmonics can worsen the vibration isolation properties at higher frequencies when driven to isolate the fundamental mode of engine vibrations. Thus, for ease of control, the fundamental mode must be as strong as possible and subsequent harmonics must be as weak as possible.

5.2 Mechanically-Blocked (Zero Displacement) Force. The measurements under mechanically-blocked conditions were performed by blocking the output pushrod with a rigid fixture. These measurements provide a measure of the maximum force that can be obtained from the actuator. As shown in Fig. 17, the MHA generates constant force over the frequency range considered. The CMA generates higher forces at the lower frequencies but the responses are nearly equal within 120 Hz to 400 Hz. Similar to the free-displacement measurements, the blocked-force order analysis is done to quantify undesired higher harmonics in the generated forces. Figures 18(*a*) and 18(*b*) show that there is not much difference between the blocked force higher harmonic components of the two devices.

5.3 Electrical Impedance and Power Requirement. The MHA is driven with unbiased sinusoidal currents while the CMA is driven with sinusoidal currents and a bias magnetic field. The power consumed by the bias field is neglected for calculation of power consumption since the bias in the CMA could also have been achieved by a permanent magnet as in the case of the MHA. Figure 19 shows the impedance of the two devices in the blocked condition. The MHA inductance is significantly lower leading to lower power consumption even when it is driven at higher current (Fig. 20). The MHA is driven at 9 A pk-pk while the CMA is driven at 6 A and 4 A pk-pk, corresponding to the specified range of input currents for the CMA.

6 Concluding Remarks

This paper presented the design, modeling and experimental characterization of a hydraulically-amplified magnetostrictive actuator for use in active engine mounts. Based on a system level mount model, the actuator stroke requirements were calculated as 1.6 mm at 20 Hz, 0.35 mm at 100 Hz, and 0.175 mm at 1000 Hz.

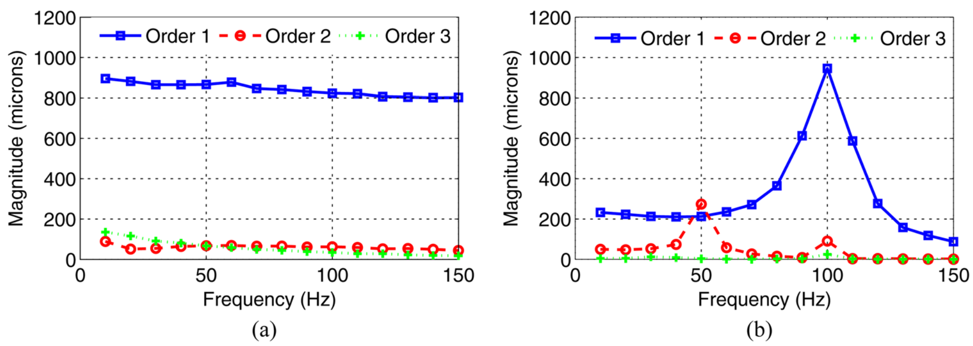

Fig. 16 Free-displacement orders of (*a*) MHA and (*b*) CMA

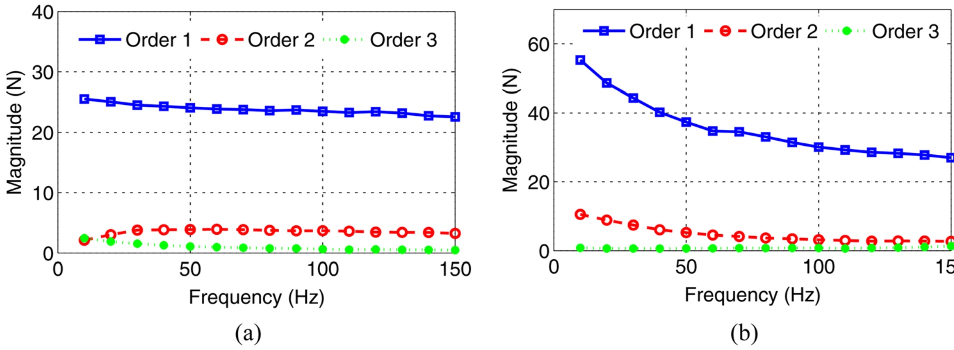

Fig. 18 Blocked force orders of (*a*) MHA and (*b*) CMA

A hydraulic gain of 69 was calculated by matching the impedance of the device and the load under idling conditions.

An efficient model for the actuator was developed based on linear piezomagnetic relations for Terfenol-D, a lumped parameter mechanical model and the LuGre friction model to describe friction at the fluid seals. Despite its simplicity, the model accurately describes the frequency domain mechanical and electrical responses of the actuator in mechanically-free and mechanically-blocked conditions, without the need for adjustable parameters. Minor discrepancies can be attributed to the assumed linear Terfenol-D material response to applied field and stress inputs, compensation of material hysteresis by LuGre friction coefficients, and unmodeled dynamic effects such as eddy currents in the magnetic circuit components.

The MHA was benchmarked against a commercial electrodynamic active mount actuator (CMA) in terms of unloaded stroke, blocked force, and electrical power consumption in the frequency range of 10 to 500 Hz. The MHA provides more than twice the bandwidth of the CMA in the unloaded stroke response and comparable force outputs in the frequency range 120 Hz to 400 Hz. Fourier analysis of the time domain displacement responses showed that the MHA has lower and flatter higher order components than the CMA, implying greater response linearity. In the future, the MHA could be optimized to reduce the compliances in the load transmission path to increase its generated force levels at lower frequencies.

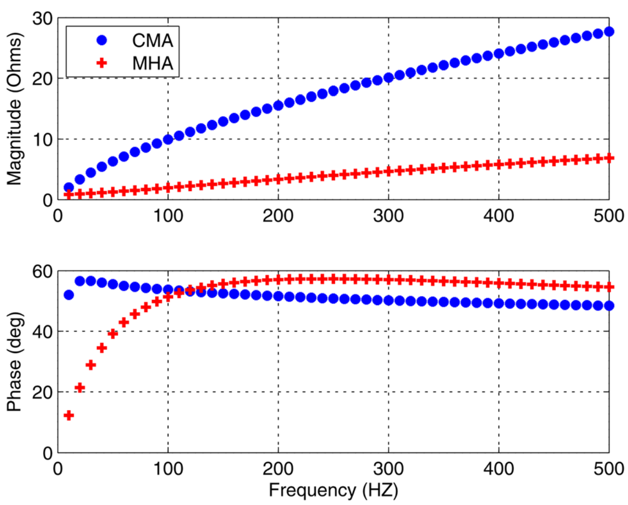

Fig. 19 Electrical Impedance of the MHA and CMA in blocked conditions

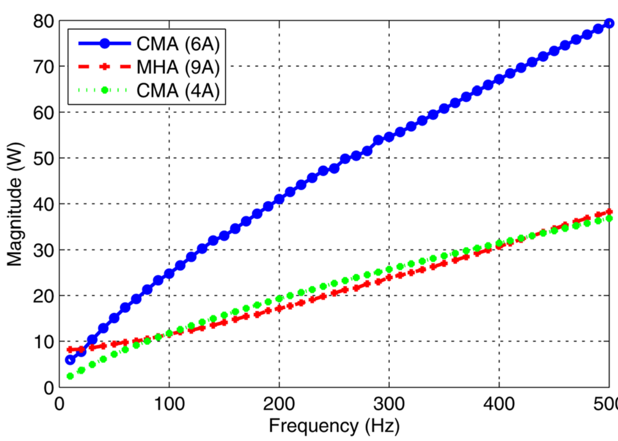

Fig. 20 Power consumption of the MHA and CMA

Acknowledgments

Support for this work comes from the member organizations of the Smart Vehicle Concepts Center (www.SmartVehicleCenter.org), the National Science Foundation Industry/University Cooperative Research Program (I/UCRC), and the Smart Vehicle Concepts Graduate Fellowship Program.

Nomenclature

A_L = cross sectional area of driven (small) piston
A_P = cross sectional area of drive (large) piston
A = cross sectional area of the Terfenol-D rod
l_a = length of the Terfenol-D rod
β = fluid's bulk modulus
β_{eff} = effective volumetric modulus of fluid and fluid chamber components
C_o = effective volumetric stiffness coefficient of the various fluid chamber components
F_a = blocked force produced by the Terfenol-D rod
I = current in the drive coil
k_{disk} = stiffness of the disk spring
k_{pre} = stiffness of the preload wave spring
k_s = stiffness of the support structure
M_L = effective mass of driven piston
M_p = effective mass of drive piston
M_s = effective mass of support
V_{ref} = volume of hydraulic fluid
σ_0 = LuGre bristle stiffness
σ_1 = LuGre bristle damping
σ_2 = LuGre viscous damping
F_c = Coulomb friction
F_s = static friction
v_s = Stribeck velocity

References

[1] Yu, Y., Naganathan, N., and Dukkipati, R., 1999, "A Literature Review of Automobile Engine Mounting Systems," Mech. Mach. Theory, **36**, pp. 123–142.

[2] Jazar, G. N., and Golnaraghi, F., 2002, "Engine Mounts for Automobile Applications—A Survey," Shock Vibr. Dig., **34**, pp. 363–379.

[3] Lee, Y., and Lee, C., 2002, "Dynamic Analysis and Control of an Active Engine Mount System," Proc. Inst. Mech. Eng. Part D, **216**, pp. 921–931.

[4] Gennesseaux, A., 1995, "A New Generation of Engine Mounts," SAE Technical Paper, No. 951296.

[5] Matsuoka, H., Mikasa, T., and Nemoto, H., 2004, "Nv Countermeasure Technology for a Cylinder-on-Demand Engine—Development of Active Control Engine Mount," SAE Trans., **113**, 2004-01-0413.

[6] Niezrecki, C., Brei, D., Balakrishnan, S., and Moskalik, A., 2001, "Piezoelectric Actuation: State of the Art," Shock Vibr. Dig., **33**, pp. 269–280.

[7] Yoon, H.-S., Washington, G., Eyabi, P., Radhamohan, M., Woodard, S. W., and Dayton, R., 2006, "A Millimeter-Stroke Piezoelectric Hybrid Actuator Using Hydraulic Displacement Amplification Mechanism," IEEE Int. Symp. Indust. Electron., **4**, pp. 2809–2813.

[8] Ellison, J., Sirohi, J., and Chopra, I., 2004, "Design and Testing of a Bidirectional Magnetostrictive-Hydraulic Hybrid Actuator," Proc. SPIE, **5390**, pp. 483–494.

[9] Bridger, K., Sewell, J. M., Cooke, A. V., Lutian, J. L., Kohlhafer, D., Small, G. E., and Kuhn, P. M., 2004, "High-Pressure Magnetostrictive Pump Development: A Comparison of Prototype and Modeled Performance," Proc. SPIE, **5388**, pp. 246–257.

[10] Rupinsky, M. J., and Dapino, M. J., 2006, "Smart Material Electrohydrostatic Actuator for Intelligent Transportation Systems," 2006 ASME International Mechanical Engineering Congress and Exposition, Proc. IMECE, **6**, pp 721–730.

[11] Mauck, L. D., and Lynch, C. S., 2000, "Piezoelectric Hydraulic Pump Development," J. Intell. Mater. Syst. Struct., **11**, pp. 758–764.

[12] Sirohi, J., and Chopra, I., 2003, "Design and Development of a High Pumping Frequency Piezoelectric-Hydraulic Hybrid Actuator," J. Intell. Mater. Syst. Struct., **14**, pp. 135–147.

[13] Ushijima, T., and Kumakawa, S., 1993, "Active Engine Mount With Piezo-Actuator for Vibration Control," SAE Trans., **102**, 930201.

[14] Shibayama, T., Ito, K., Gami, T., Oku, T., Nakajima, Z., and Ichikawa, A., 1995, "Active Engine Mount for a Large Amplitude of Engine Vibration," SAE conference proceedings, 951298.

[15] Holt, J., Rao, M., Blough, J., and Gruenberg, S., 2007, "Time History-Based Excitation in the Dynamic Characterization of Automotive Elastomers," Proc. IMechE Part D, **221**, pp. 271–284.

[16] Ohadi, A., and Maghsoodi, G., 2007, "Simulation of Engine Vibration on Nonlinear Hydraulic Engine Mounts," J. Vibr. Acoust., **129**, pp. 417–424.

[17] Kyprianou, A., Giacomin, J., Worden, K., Heidrich, M., and Bocking, J., 2000, "Differential Evolution Based Identification of Automotive Hydraulic Engine Mount Model Parameters," Proc. Instn. Mech. Eng., **214**, pp. 249–264.

[18] Singh, R., 2009, personal communication.

[19] Giurgiutiu, V., Chaudhry, Z., and Rogers, C., 1995, "Stiffness Issues in the Design of Isa Displacement Amplification Devices," Proc. SPIE, **2443**, pp. 105–119.

[20] Olsson, H., Astrom, K. J., de Wit, C. C., Gafvert, M., and Lischinsky, P., 1998, "Friction Models and Friction Compensation," Eur. J. Control, **4**(3), pp. 176–195.